Available online at www.sciencedirect.com
ScienceDirect
Nuclear Instruments and Methods in Physics Research A 588 (2008) 359–374
NUCLEAR INSTRUMENTS & METHODS IN PHYSICS RESEARCH Section A
www.elsevier.com/locate/nima

Spatial and temporal beam profile monitor with nanosecond resolution for CERN's Linac4 and Superconducting Proton Linac

M. Hori[a,b,c,*], K. Hanke[c]

[a]Max-Planck-Institut für Quantenoptik, Hans-Kopfermann-Strasse 1, D-85748 Garching, Germany
[b]Department of Physics, University of Tokyo, 7-3-1 Hongo, Bunkyo-ku, Tokyo 113-0033, Japan
[c]CERN, CH-1211 Geneva 23, Switzerland

Received 1 January 2008; received in revised form 3 January 2008; accepted 4 January 2008
Available online 31 January 2008

Abstract

The Linac4, now being developed at CERN, will provide 160-MeV H^- beams of high intensity $N = 2 \times 10^{14}$ ions s^{-1}. Before this beam can be injected into the CERN Proton Synchrotron Booster or future Superconducting Proton Linac for further acceleration, some sequences of 500-ps-long micro-bunches must be removed from it, using a beam chopper. These bunches, if left in the beam, would fall outside the longitudinal acceptance of the accelerators and make them radioactive. We developed a monitor to measure the time structure and spatial profile of this chopped beam, with respective resolutions $\Delta t \sim 1$ ns and $\Delta x \sim 2$ mm. Its large active area 40 mm × 40 mm and dynamic range also allows investigations of beam halos. The ion beam first struck a carbon foil, and secondary electrons emerging from the foil were accelerated by a series of parallel grid electrodes. These electrons struck a phosphor screen, and the resulting image of the scintillation light was guided to a thermoelectrically cooled, charge-coupled device camera. The time resolution was attained by applying high-voltage pulses of sub-nanosecond rise and fall times to the grids. The monitor has been tested with 700-ps-long UV laser pulses, and a 3-MeV proton beam. Its response over a wide range of beam intensities between $N_e \sim 5$ and 4×10^8 electrons emitted from the foil per pulse was studied. The monitor can also be used to measure the profiles of antiproton beams in the future facilities of Facility for Low-energy Antiproton Ion Research (FLAIR) or Extra Low Energy Antiproton Ring (ELENA).
© 2008 Elsevier B.V. All rights reserved.

PACS: 41.85.Qg; 41.85.Ew; 07.77.Ka; 29.40.Gx

Keywords: Beam profile monitor; Halo monitor; Secondary electron emission; Beam chopper

1. Introduction

The planned Linac4 facility [1,2] of CERN will provide H^- beams of energy $E = 160$ MeV and a high intensity $N = 2 \times 10^{14}$ ions s^{-1}. This beam will be sequentially accelerated by the CERN Proton Synchrotron Booster (PSB), Proton Synchrotron (PS), and Super Proton Synchrotron (SPS), before being injected into the Large Hadron Collider (LHC) for proton–proton collisions at a center-of-mass energy $E = 14$ TeV. Linac4 is important in achieving [3] the highest possible beam current ($I \sim 0.9$ A) in the LHC. The beam intensity delivered to LHC can be further increased by factor ~2, by replacing the PSB and PS with a 4–5-GeV Superconducting Proton Linac (SPL) [4] and a 50-GeV PS2 [3]. The first section of Linac4, which accelerates the beam to $E = 3$ MeV and chops its time structure (Fig. 1), is now being constructed at CERN. In this paper, we describe a monitor which characterizes the time evolution of the spatial profile of this beam. It is based on the imaging of secondary electrons emitted from a thin target foil.

In the planned design of Linac4 (Table 1, Fig. 1), a H^- beam of energy $E = 45$ keV is extracted from a duoplasmatron source and traverses a Low-Energy Beam Transport (LEBT). It is then accelerated to $E = 3$ MeV in a Radiofrequency Quadrupole (RFQ) which is excited at

*Corresponding author at: CERN, CH-1211 Geneva 23, Switzerland. Tel.: +41 22 767 8306; fax: +41 22 767 3500.
E-mail address: Masaki.Hori@cern.ch (M. Hori).

0168-9002/$ - see front matter © 2008 Elsevier B.V. All rights reserved.
doi:10.1016/j.nima.2008.01.078

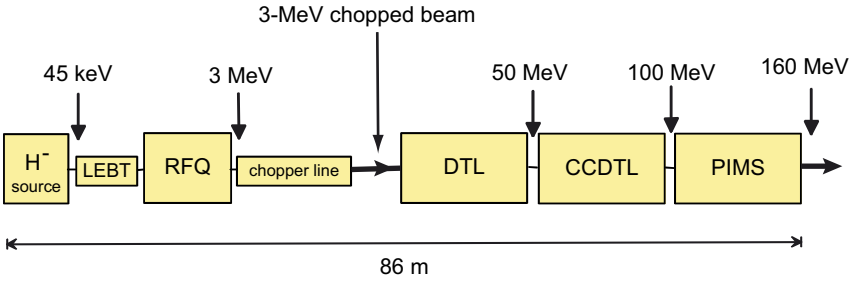

Fig. 1. Schematic layout of Linac4: its acceleration components and output energies. The H^- ions produced by the ion source are transported through the Low-Energy Beam Transport (LEBT). They are then accelerated by the Radiofrequency Quadrupole (RFQ), Drift Tube Linac (DTL), Cell-Coupled Drift Tube Linac (CCDTL), and Pi-Mode Structure Linac (PIMS). Note position of the chopped 3-MeV beam downstream of RFQ [1].

Table 1
Some beam parameters of the Linac4 and its RFQ

	RFQ	Linac4
Output energy	3 MeV	160 MeV
Micro-bunch frequency	352.2 MHz	
Micro-bunch length	500 ps	
Macro-pulse length	400 μs	
Macro-pulse rep rate	2 Hz	
Macro-pulse current	70 mA	40 mA
Average current	56 μA	32 μA
Particles per micro-bunch	1.1×10^9	
Particles per macro-pulse	1.8×10^{14}	1.0×10^{14}
Beam diameter	~10 mm	

The monitor will be positioned downstream of a beam chopper (Fig. 1) and used to measure the time and spatial profiles of the 3-MeV RFQ beam. From Ref. [1].

frequency $f_e = 352.2\,\text{MHz}$. The beam exiting the RFQ output consists of macro-pulses of duration $\Delta t_m = 400\,\mu\text{s}$ and current $I_m = 70\,\text{mA}$ which arrive at a repetition rate $f_r = 2\,\text{Hz}$, corresponding to an average beam current $I_a = I_m \Delta t_m f_r \sim 60\,\mu\text{A}$. Each macro-pulse consists of a train of 500-ps-long micro-bunches that are spaced by intervals $f_e^{-1} = 2.8\,\text{ns}$. Each macro-pulse and micro-bunch, respectively contain 10^{14} and 10^9 H^- ions (Table 1). This beam is further accelerated to $E = 160\,\text{MeV}$ by traversing the Drift Tube Linac (DTL), Cell-Coupled Drift Tube Linac (CCDTL), and Pi-Mode Structure Linac (PIMS). It is then injected into the PSB using a charge-exchange method [5].

During the acceleration phase for Linac4 injection into PSB, a beam chopper [1,6] positioned downstream of the RFQ removes 133 consecutive micro-bunches out of every 352 in the beam. It is here crucial to remove all the ions in these bunches, as the ions would otherwise fall outside the longitudinal acceptance of the PSB, strike its inner walls, and activate the accelerator.

The precise control of the transverse beam profile is also important for proper acceleration of the beam. At the high intensities of Linac4, a variety of (e.g., space-charge and resonant oscillation) effects can easily cause halos [7–9] to form around the core of the beam. These effects will be especially strong during the first stages of the acceleration to $E = 3\,\text{MeV}$ in the RFQ [1]. Simulations [10,11] predict that the halo at the RFQ exit would constitute $\geqslant 10^{-4}$ of the main beam. Unless this halo is properly diagnosed and removed, it will be accelerated with the main beam, eventually striking the walls of the accelerator, and thereby leading to further activation.

The monitor described herein will measure the spatial and time profiles of the 3-MeV beam, to diagnose whether or not they satisfy the above criteria on the beam chopping and halo. For this task a monitor of high time and spatial resolution ($\Delta t \sim 1\,\text{ns}$ and $\Delta x \sim 2\,\text{mm}$), large dynamic range ($> 10^5$), and active area ($40\,\text{mm} \times 40\,\text{mm}$) is needed. The monitor must be robust, so that it can be routinely operated with minimum maintenance.

If Linac4 is to be used in conjunction with the future SPL, its beam quality must be even higher than that described above in terms of beam halo and timing structure [4]. The chopper frequency will here be increased, so that three consecutive micro-bunches out of every eight are removed. Experiments at the Spallation Neutron Source (SNS) linac of ORNL [9,12] have revealed that any beam loss at such a facility must be kept below a value equivalent to power $P = 1\,\text{W}$ dissipated per meter of accelerator, if the activation is to be maintained within acceptable limits. Simulations show that this corresponds to less than $\sim 10^3$ ions lost per micro-bunch, in the halo and chopped part of the Linac4 beam [1]. For the monitor to properly diagnose this, it must detect a weak pulse containing 10^3 ions, without being blinded by the much stronger pulse of 10^9 ions that lies nearby. This is difficult, since the two pulses are here temporally and spatially separated by only $f_e^{-1} = 2.8\,\text{ns}$ and $\sim 10\,\text{mm}$. In this paper, we also studied whether the monitor can be used in this SPL-quality beam.

Linac4 is in the early stages of construction, and H^- beams of comparable energy, intensity, and time structure were not readily available to us. We, therefore, tested the monitor by irradiating the target foil with UV laser pulses of short ($\Delta t \sim 700\,\text{ps}$) duration, and imaging the photoelectrons that were emitted, the laser intensity being adjusted to generate the electron flux ($N_e \sim 4 \times 10^8$ emitted per micro-bunch) expected at Linac4. The monitor was also tested against 3-MeV proton beams of low intensity (between $N_p = 10$ and 6×10^4 particles per micro-bunch), which simulated the halo of the Linac4 beam.

Beam monitors based on secondary electron emission from wire electrodes [13] are now used at the Antiproton Decelerator (AD) of CERN to measure the profiles of beam pulses containing $N_{\bar{p}} \sim 10^6 - 10^7$ antiprotons, with energies between $E = 100\,\text{keV}$ [14] and 5 MeV [15]. These wire monitors [13] measured the spatial profile by intercepting ~2% of the beam, while allowing most of the antiprotons to pass through without degradation. These devices, however, are unable to measure low beam intensities $N_{\bar{p}} < 10^4$. The foil monitor described in this paper has a much higher sensitivity and dynamic range. It may thus be preferable to use them in some beamlines, at the future Extra Low Energy Antiproton Ring (ELENA) [16,17] at CERN, or Facility for Low-energy Antiproton and Ion Research (FLAIR) [18] at GSI.

2. Monitor principle

In the present monitor, the H^- ions were allowed to strike a carbon foil of thickness $t_d = 50\,\mu g\,cm^{-2}$ (Fig. 2). The secondary electrons emitted from the foil were moved out of the path of the H^- beam [19–21] and collected on a phosphor screen [22,23]. The image of the resulting scintillation light propagated along a fiber optic conduit [24] and was photographed by a Charge-Coupled Device (CCD) camera. CCDs and phosphor screens are normally used as integration devices because of their ms-scale response times; in the present monitor, however, a resolution $\Delta t \sim 1$ ns was attained by applying high voltage (HV) pulses of sub-nanosecond rise or fall times on a grid electrode and the phosphor screen. The grids controlled the flow of secondary electrons from the foil to the phosphor [25,26]. The monitor could thus be gated off during the strong H^- micro-bunches and turned on within ~500 ps to verify whether there were any residual particles in the chopped bunches. The CCD normally had a dynamic range of $\sim 10^4$ with respect to single micro-bunches of the beam. This range could be further increased by many orders of magnitude, by exposing the CCD over several micro-bunches.

Among the reasons why we chose this design was its large dynamic range, robustness against high-intensity beams [22], and ease by which it could be operated and gated on and off with sub-nanosecond-scale response times. Many groups have constructed profile monitors, wherein secondary electrons emitted from foils were multiplied using Microchannel Plates (MCPs). The electrons were then imaged using a phosphor screen [22,23,27], segmented electrodes [28,29], delay-line anodes [30–32], or resistive charge-division [33,34] anodes. These MCP-based monitors were mainly designed for low beam intensities, where the hits of individual particles could be resolved. Since MCPs quickly saturate [35] at higher intensities, however, they were not used in the present work. We instead relied on a thermoelectrically cooled CCD, which could be exposed for many minutes to provide the high sensitivity and dynamic range needed here.

Past studies have measured beam halos in many ways. In one popular method, a filament, slit, or scraper electrode was mounted on a motorized platform and scanned through the halo [36–38]. The induced current on the electrode was then measured, to derive the intensity and spatial profile of the halo. An alternate method measured the beam profile by detecting the increase of the filament temperature when the beam struck it [39]. This temperature was derived by measuring the characteristic oscillation frequency of the filament. Several groups [40–43] have measured the spatial profile of H^- beams by irradiating the

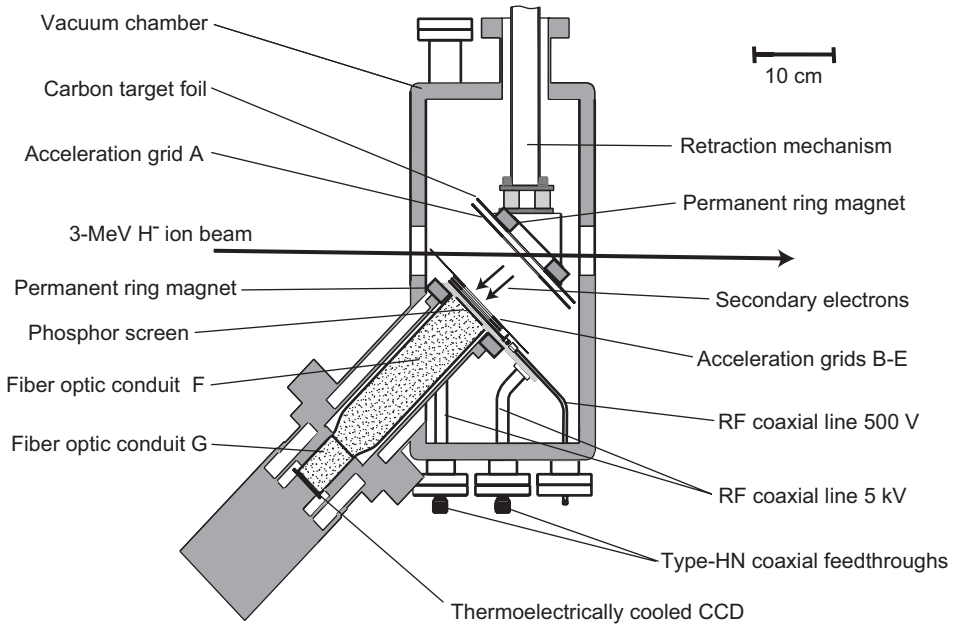

Fig. 2. Schematic layout of the beam profile monitor. Incident H^- ions of energy $E = 3$ MeV struck a carbon target foil. Secondary electrons emitted from the foil were accelerated by grids A–E and struck a phosphor screen. The fluorescence image was transported by fiber optic conduits F and G to a CCD.

ions with a Nd:YAG laser pulse, and photoneutralizing them. The emerging electrons or neutral hydrogen atoms were then detected. In another method, the beam was allowed to ionize the residual gas in the accelerator, and the spatial profile of the emerging electrons were imaged [44–47]. All these detectors may be used in Linac4. The monitor described in this paper was intended to complement these existing techniques, with the ability to provide "stopped-action photographs" of the beam with a large active area 40 mm × 40 mm, and high time resolution $\Delta t \sim 1$ ns.

3. Monitor construction

The monitor (Fig. 2) was housed in a 490 mm × 460 mm × 260 mm rectangular vacuum chamber made of type 316L non-magnetic stainless steel. The length of the monitor along the beam path was kept as short as possible ($l = 260$ mm), so that any adiabatic increase in the emittance of the H^- beam traveling through the monitor would be minimized. Before operation, the chamber was baked to temperature $T = 70\,^\circ$C. Turbo and ion pumps of pumping speed $s = 300$ and $600\,l\,s^{-1}$ were then used to reach a vacuum $P \sim 5 \times 10^{-7}$ Pa. A graphite carbon foil (manufactured by Arizona Carbon Foil Co.) of size 60 mm × 50 mm was suspended in the center of the chamber, at a 45° angle with respect to the H^- beam. Its thickness $t_d \sim 50\,\mu g\,cm^{-2}$ corresponded to a small energy loss $\Delta E < 10$ keV from 3-MeV protons, thus ensuring that the heat deposited in the foil by the beam would be minimized. During the measurements using the pulsed UV laser beam, the carbon foil was replaced by a gold photocathode of $t_d = 100\,\mu$m. These foils were mounted on a stainless steel electrode measuring 200 mm × 180 mm and could be moved in and out of the H^- beam using a translation stage.

A grid (labeled A in Fig. 2) was positioned parallel to the carbon foil at a distance $l \sim 7$ mm from it, and in the path of the H^- beam. It consisted of 25 graphite filaments of diameter $d = 5\,\mu$m (manufactured by Toray Industries K.K.), which were stretched over a conductive frame with a pitch $p_t = 3$ mm between neighboring filaments. A 60 mm × 80 mm rectangular hole was cut in the center of the frame to allow the passage of the secondary electrons. The grid was manufactured [48] by first depositing gold layers of thickness $t_d = 15\,\mu$m on the two sides of a ceramic frame, using a thick-film printing method with a silk screen. The filaments were stretched over the frame with a mechanical tension $g = 1$ g, and their two ends glued on the gold surface using a conductive epoxy resin. Similar filaments are widely used in wire scanners [49–51] that measure mA-scale beams. Calculations showed that they would heat up ($T > 2000\,^\circ$C) and break, if the full RFQ beam intensity of $I = 70$ mA were focused into a 1-mm-diameter spot on their surface. The filaments would easily survive at $d \sim 10$ mm and reduced values of the duration $\Delta t_m \sim 100$ ns and repetition rate $f_r \leqslant 1$ Hz of the RFQ macro-pulses.

The secondary electrons traversed a 65-mm-long drift region, which moved them out of the path of the H^- beam. They reached a stack of four grids B–E placed parallel to the carbon foil. Each grid consisted of 25 gold-coated tungsten wires of diameter $d = 10\,\mu$m and pitch $p_t = 2$ mm, mounted on a ceramic frame with a 50 mm × 50 mm rectangular hole in the center. Grids B, C, and E were constructed by printing gold layers of thickness $t_d = 30\,\mu$m on the ceramic frames, and the wires were stretched over the frame with a tension $g = 10$ g. The two ends of each wire were pressed onto the gold-coated frames with several hundred grams of force, using an electrode tip made of tungsten [13]. The wires were embedded and fused into the gold by applying a pulsed current on this tip.

Grid D (Fig. 3(a)) had a more complicated structure which allowed 1-kV pulses of sub-nanosecond fall time to be applied to it. The grid surface of 50 mm × 50 mm was segmented into four 12.5 mm × 50 mm strips, parallel to the wires. The segments were connected to four gold striplines printed on the ceramic frame, their widths and

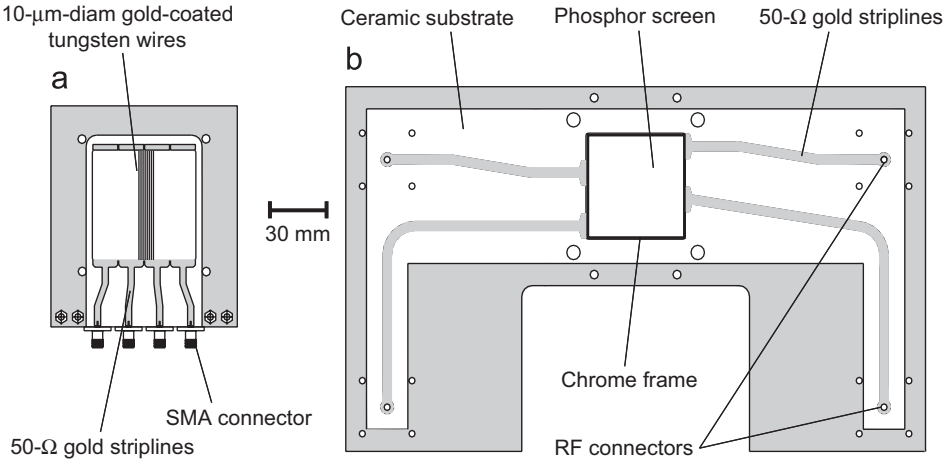

Fig. 3. Top view of grid D, showing four striplines of impedance $Z_0 = 50\,\Omega$ used to apply a voltage pulse of amplitude $V = -1$ kV to the grid with a fall time of $t_r \sim 700$ ps (a). Top view of the phosphor screen, with four striplines used to apply a 6-kV pulse of rise time $t_r \sim 500$ ps (b).

thicknesses adjusted to attain a characteristic impedance $Z_0 = 50\,\Omega$. Subminiature version A (SMA) connectors were soldered on the end of each stripline using a fluxless, indium-tin solder. Semi-rigid coaxial cables were fixed to the connectors, and these lines traversed the chamber walls to the outside via SMA vacuum feedthroughs. The grid potential could thus be driven without impedance mismatch by the four parallel lines [52–57], with a combined impedance $Z_0 \sim 12\,\Omega$.

The phosphor screen [58–61] was manufactured by first depositing a transparent and conductive layer of indium tin oxide (ITO, produced by Proxitronic GmbH) on the surface of a 50 mm × 50 mm fiber optic plate (manufactured by Schott Fiber Optics Inc.) of thickness $t_d = 3$ mm (Fig. 3(b)). The plate consisted of 6-μm-diameter optical fibers made of type Schott 47A glass, which were bundled together. It contained interstitial extra-mural absorption (EMA) glass, i.e., black glass fibers inserted in the spaces between the clear ones [24]. These absorbed the stray light in the cladding, thereby reducing the cross talk between the fibers and increasing the contrast of the transmitted image. A sedimentation method was then used to deposit 1-μm-diameter grains of gadolinium oxysulphide doped with terbium (Gd_2O_2S: Tb, P43) on the plate. This phosphor [58] emitted scintillation light with a wavelength distribution $\lambda = 360-680$ nm, with a maximum at $\lambda = 545$ nm. The 90%-to-10% and 10%-to-1% decay times for the light were $\tau = 1$ and 1.6 ms. A 40-nm-thick aluminum layer was next evaporated on the phosphor. This layer served three purposes: (i) only those electrons accelerated to energy $E > 3$ keV could penetrate the layer and produce scintillation light, whereas lower-energy electrons were stopped by it. The detector could thus be quickly turned on or off by adjusting the incident energy of the secondary electrons, (ii) it prevented stray light, or the glow from the carbon foil heated by the H^- beam, from entering the fiber optic bundle, and (iii) it increased the collection efficiency of the fluorescence light. The manufacturer claimed that the photon yield of similar phosphor screens against a 6-keV electron was around ~200.

A chrome electrode of 1-mm width was sputtered around the outer edges of the phosphor screen. The screen was then mounted on a larger ceramic frame of size 200 mm × 150 mm and thickness $t_d = 3$ mm (Fig. 3(b)). As in the case of grid D, four gold striplines of impedance $Z_0 = 50\,\Omega$ were printed on the ceramic and connected to the chrome edges of the phosphor screen. The other ends of the striplines were connected to 16-mm-diameter coaxial lines of $Z_0 = 50\,\Omega$, made of copper. The combined impedance of the four lines was thus $Z_0 = 12\,\Omega$. This allowed a voltage pulse of amplitude 6–7 kV and rise-time $t_r \sim 500$ ps to be applied on the phosphor screen, by driving the four cables simultaneously. The pulses entered the vacuum chamber through type-HN coaxial feedthroughs.

The image of the scintillation light was transmitted along a 230-mm-long, 60-mm-diameter fiber optic conduit (F in Fig. 2), attached to the reverse side of the phosphor screen. The conduit consisted of 10-μm-diameter optical fibers made of type Schott 24A glass, with a numerical aperture of ~1.0 and including interstitial EMA as in the case of the phosphor screen above. The conduit tapered off to a diameter $d = 40$ mm at its end; thus any image transmitted through it was demagnified by a factor of 1.5. The exit side of conduit F was attached to another conduit G of diameter $d = 40$ mm and length $l = 70$ mm. Conduit G traversed an O-ring vacuum seal, and guided the scintillation light out of the monitor chamber. Its exit side was glued to the surface of a 26.8 mm × 26.0 mm CCD sensor (Princeton Instruments SCX-1300 camera with EEV CCD36-40 sensor), which had 1340 × 1300 pixels of resolution $\Delta x = 20$ μm. The CCD was thermoelectrically cooled to temperature $T \sim -40\,^\circ$C, so that the dark current and readout noise per pixel were $< 1\,e^-\,s^{-1}$ and $\leqslant 5\,e^-$, respectively. It could thus be exposed for many minutes, with negligible effects of the dark current. The quantum efficiency of the CCD in the emission range of the P43 phosphor was 20–40%. This indicated that the monitor should in principle be able to detect pulsed beams containing < 100 H^- ions, if the CCD were exposed over several such pulses.

We were initially concerned that the slow ($\tau \sim 1$ ms) response time of the P43 phosphor would cause strong afterglows, that would prevent measurements of the time profile of H^- pulses with nanosecond-scale resolutions. We therefore tested phosphor screens of yttrium silicate doped with cerium (Y_2SiO_5: Ce, P47), which had faster 90%-to-10% and 10%-to-1% decay times ($\tau = 100$ ns and 2.9 μs, respectively). Due to the low quantum efficiency of the CCD at the P47 emission wavelengths $\lambda = 370-480$ nm, however, the resulting images were an order of magnitude dimmer than those obtained using P43. We therefore used the later in all the experiments described below. Despite the 1-ms response time of P43, the electronic gating of the grids and phosphor screen provided an adequate time resolution $\Delta t \sim 1$ ns, as described below.

During some of the measurements, ring magnets made of strontium ferrite were positioned behind the target foil and phosphor screen, as shown in Fig. 2. The magnets had outer and inner diameters of $d = 100$ and 70 mm, and produced an axial field $B \sim 100$ Gauss between the foil and phosphor screen. This is similar to the configuration used in Ref. [21]. Due to outgassing from these magnets, the vacuum deteriorated to $P \sim 5 \times 10^{-6}$ Pa when they were installed.

4. Monitor operation

In Fig. 4, a schematic diagram of the electronics used to apply pulsed and DC voltages sequentially to the monitor electrodes are shown. Table 2 lists three settings 1–3 of the potentials, which were applied to the carbon foil (denoted by V_f), grids A–E (denoted by $V_A - V_E$), and the phosphor screen (V_p) during each sequence. Henceforth, we take the

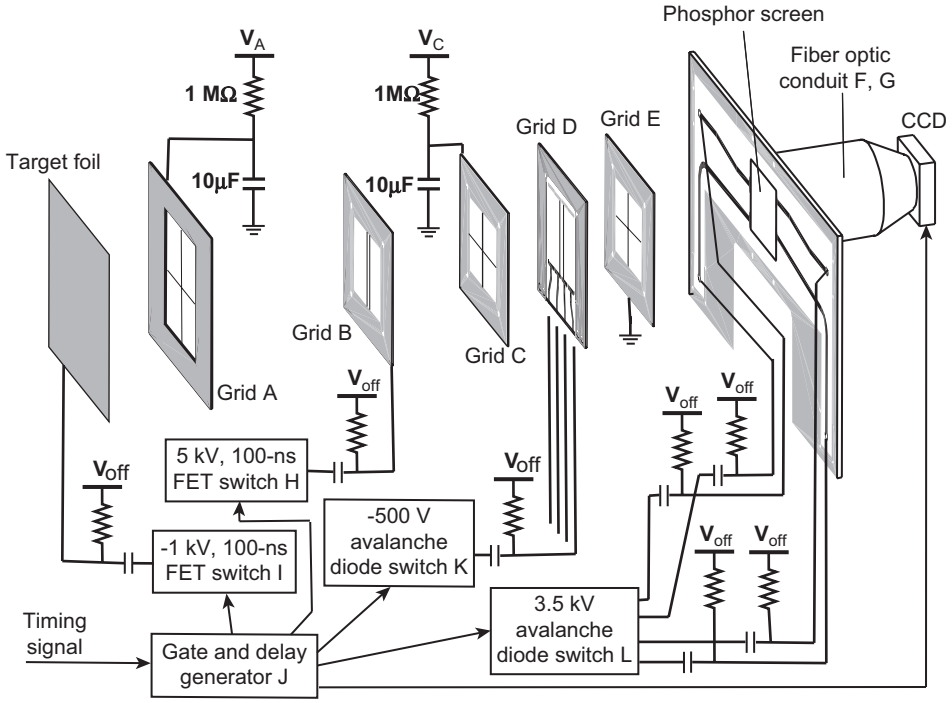

Fig. 4. Schematic diagram of the electronics used to apply the DC and pulsed voltages on the target foil, grids A–E, and phosphor screen. A timing signal from the accelerator triggered the gate-and-delay generator J. Its five outputs then triggered the CCD, the two FET switches H and I, and the two avalanche diode switches K and L.

Table 2
Three sets of voltage settings applied to the target foil, grids A–E, and phosphor screen during operation of the beam profile monitor (see text)

	Foil V_f (kV)	Grid A V_A (kV)	Grid B V_B (kV)	Grid C V_C (kV)	Grid D V_D (kV)	Grid E V_E (kV)	Phosphor V_p (kV)
Settings 1, *for high spatial resolution, no magnetic field* ($B = 0$)							
Gated off	1.1	2.0	−0.3	0.2	−0.2	0	0.3
Initial accel.	−3.0	2.0	5.0	0.2	−0.2	0	0.3
Phosphor on	−3.0	2.0	5.0	0.2	−0.2	0	6.5
Phosphor off	−3.0	2.0	5.0	0.2	−1.2	0	6.5
Settings 2, *for measurements using the magnetic field* $B = 100$ *Gauss*							
Gated off	1.1	1.0	−0.3	−0.1	−0.2	0	0.1
Initial accel.	−0.3	1.0	5.0	−0.1	−0.2	0	0.1
Phosphor on	−0.3	1.0	5.0	−0.1	−0.2	0	6.5
Phosphor off	−0.3	1.0	5.0	−0.1	−1.2	0	6.5
Settings 3, *for minimum pre- and afterpulsing. No magnetic field* ($B = 0$)							
Gated off	0.8	0.4	−0.3	−0.1	−0.1	0	0.1
Initial accel.	−0.2	0.4	5.0	−0.1	−0.1	0	0.1
Phosphor on	−0.2	0.4	5.0	−0.1	−0.1	0	5.0
Phosphor off	−0.2	0.4	5.0	−0.1	−1.1	0	5.0

example of the voltage settings three in Table 2 to describe the monitor operation.

The sequence proceeded as follows: (i) *CCD exposure start*, the accelerator or Nd:YAG laser provided a timing signal in coincidence with the arrival of the ion or laser pulse at the monitor. This triggered a gate-and-delay generator (Stanford Research Systems DG535, denoted by J in Fig. 4). The delays in its four output channels, relative to the trigger, were programmed with a resolution $\Delta t = 100$ ps. One of these outputs triggered the CCD and started the exposure, (ii) *gate off*, the monitor was normally gated "off" by applying an electric field between the carbon foil and grids A and B (e.g., $V_f = 0.8$ kV and $V_A = 0.4$ kV), such that the secondary electrons emitted from the carbon foil would be reabsorbed by it (Table 2), (iii) *initial acceleration*, the delay generator next triggered a bipolar Field Effect Transistor (FET) switch (denoted by I in Fig. 4, manufactured by Behlke Power Electronics GmbH), which applied a 100-ns-long voltage pulse with an amplitude of −1 kV, and rise- and fall times of $t_r \sim 20$ ns

to the target foil. The bipolar FET switch H was also triggered, which switched the potential on grid B to $V_B = 5\,\mathrm{kV}$. This caused the electrons emitted from the target foil to be accelerated towards the phosphor screen. In Figs. 5(a) and (b), the waveforms of these two pulses measured using an oscilloscope (Lecroy Wavepro 7300A) of analogue bandwidth $f = 3\,\mathrm{GHz}$ and digital sampling rate $f = 10\,\mathrm{GHz}$, and a voltage divider placed near the output of the FET switches, are shown. The electrons arriving at the phosphor had low-kinetic energies ($E < 1\,\mathrm{keV}$), and so they were absorbed by the aluminum layer on the screen and did not produce fluorescent light.

The remainder of the sequence was as follows: (iv) *fluorescence on*, avalanche diode switch L [62] (Kentech Instruments PBG3/s/v) was triggered at $t = t_L$, and this produced HV pulses of amplitude $V = 3.5\,\mathrm{kV}$ and rise time $t_r \sim 200\,\mathrm{ps}$ on its four $Z_0 = 50\text{-}\Omega$ outputs. The pulses returned to the baseline within $\Delta t \sim 30\,\mathrm{ns}$. The pulses propagated along four parallel coaxial cables of length $l = 2\,\mathrm{m}$, and arrived simultaneously at the phosphor screen. In Fig. 5(d), the oscilloscope trace of this HV pulse, measured using a voltage divider installed at the output of switch L, is shown. An expanded view of the rising edge of the pulse is shown in Fig. 6(a). As the phosphor screen presented an open circuit at the end of the coaxial lines, it reflected the voltage pulses, which then returned to switch L. This caused the two-peak structure shown in Fig. 5(d). At the position of the phosphor screen, the leading edge of the reflected pulse overlapped with the counterpropagating trailing edge [52], and this collision caused the potential on the phosphor screen to double its amplitude, to $V \sim 6\,\mathrm{kV}$. Measurements indicate that the actual rise time of the potential [27] on the phosphor screen was around $t_r \sim 500\,\mathrm{ps}$. The electrons were now accelerated to the energies needed to penetrate the aluminum layer and produce fluorescent light, (v) *fluorescence off*, avalanche diode switch K (Kentech Instruments HMP1/s/v) was next triggered at $t = t_K$. This simultaneously generated HV pulses of amplitude $V = -500\,\mathrm{V}$ and fall time $t_r \sim 200\,\mathrm{ps}$ on the four lines connected to grid D (Fig. 6(b)). As in the phosphor case above, the two-pulse structure from the cable reflection can be seen in Fig. 5(c). This reflection induced a pulse of amplitude $V = -1\,\mathrm{kV}$ on the grid, with a measured fall time of $t_r \sim 700\,\mathrm{ps}$. The potential barrier on grid D now prevented the electrons from reaching the foil.

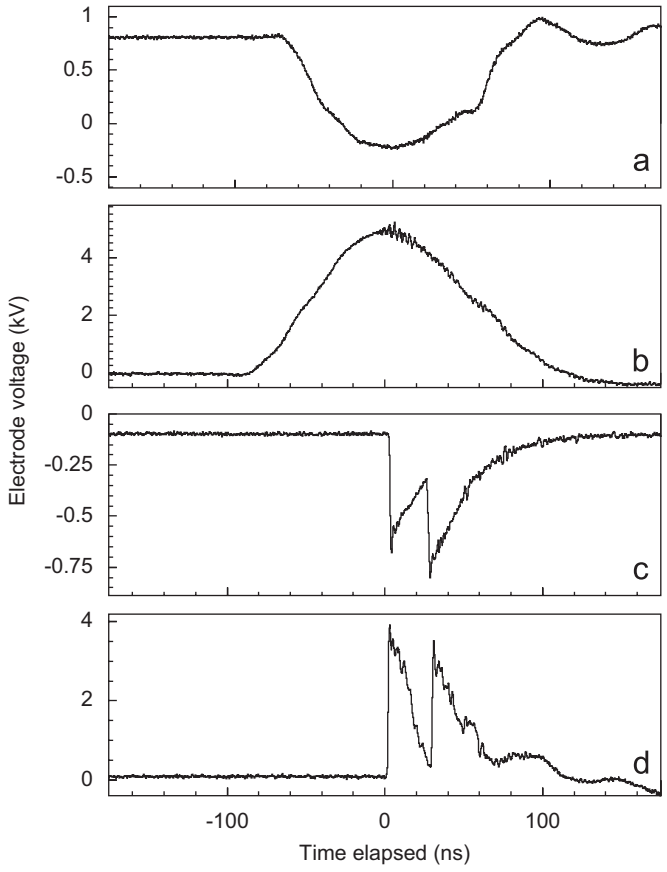

Fig. 5. Oscilloscope traces of the voltage pulses applied to the target foil (a), grid B (b), grid D (c), and the phosphor screen (d). They were measured using voltage dividers located at the output of the FET or avalanche diode switches. The double-pulse structure seen in (c) and (d) were caused when the voltage pulses reflected from the electrodes, and counterpropagated down the coaxial lines back to the voltage switches. Due to this reflection, the voltage amplitudes induced on grid D and the phosphor screen were factor ~2 larger than the values shown in these traces (see text).

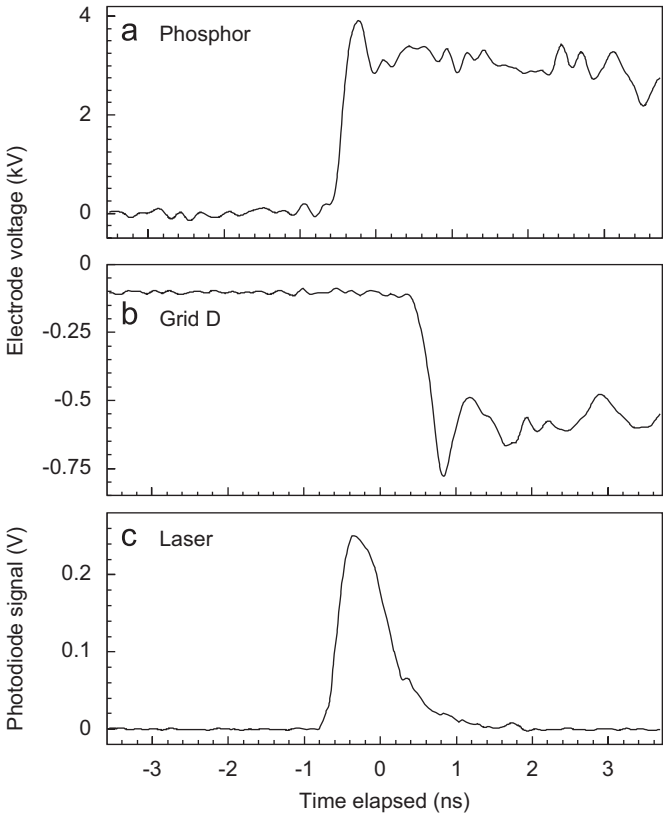

Fig. 6. Enlarged portions of the fast pulses applied to grid D (a) and the phosphor screen (b). Note rise and fall times $t_r = 200\,\mathrm{ps}$ of the pulses. The time profile of the SBS laser pulse measured using a p–i–n photodiode (c). Its arrival timing was adjusted to coincide with the gate of the profile monitor.

The relative timing between the HV pulses generated by switch K and L defined the interval ($t_K - t_L < 1$ ns in the case of Fig. 6) during which the phosphor emitted light. The above steps (ii)–(v) could be repeated to integrate the signals from several H^- pulses on the CCD, (vi) *readout*, the CCD exposure was stopped and the pixels read out.

5. Generation of sub-nanosecond UV laser pulses

We next generated UV laser pulses of energy $E \sim 5$ mJ, wavelength $\lambda = 266$ nm, and pulse length $\Delta t \sim 700$ ps, to simulate the time structure of the micro-bunches in Linac4. Since the Q-switch Nd:YAG laser (Coherent Infinity) used here produced 4-ns-long laser pulses, we used a stimulated Brillouin scattering (SBS) cell [63–65] to temporally compress them. This laser system (Fig. 7) was originally designed [66] for use in laser spectroscopy experiments of antiprotonic helium atoms [67] and ions [68]. Since the cavity of this Nd:YAG laser was injection-seeded with a continuous-wave ring laser, its output beam of $E = 600$ mJ and $\lambda = 1064$ nm had smooth time and spatial profiles, and a single longitudinal mode. This beam was first passed through a 8-mm-long, beta-barium borate (BBO) crystal cut for type-I frequency conversion (denoted by A in Fig. 7), thereby producing a 532-nm beam of $E = 280$ mJ and a horizontal polarization. Two plano-convex lenses arranged in a relay-imaging configuration then transferred the beam image to the position of the SBS cell. This ensured that the beam profile in the SBS cell was smooth, which was an essential condition in attaining a high mode quality in the SBS beam. Before entering the SBS amplifier cell, the laser pulse traversed a thin-film polarizing beam splitter and a Fresnel Rhomb, thus becoming circularly polarized. A Galilean telescope installed at the entrance of the cell then produce a parallel beam of diameter $d \sim 9$ mm and $E \sim 200$ mJ in the cell.

The SBS amplifier cell was similar to the one described in Ref. [65]. Polished windows of thickness $t_d = 8$ mm, made of UV-transparent fused silica (Suprasil P-20, manufactured by Shin-Etsu Quartz Products Co.), were bonded on the two ends of a quartz tube of diameter $d = 40$ mm and length $l = 1.2$ m. Deionized water was circulated through the cell using a centrifugal pump of flow rate $s \sim 2\,\mathrm{l\,min^{-1}}$. The water was continuously filtered through a cartridge of sintered polypropylene of pore size $p_s \sim 0.2\,\mu$m. The laser beam underwent Rayleigh scattering in the water, and some of this scattered light was guided along the cell by reflecting off the tube walls. To block this light and prevent it from superimposing itself onto the compressed laser beam, 10 quartz diaphragms of inner diameter $d = 20$ mm and thickness $t_d = 2$ mm were fused along the inside of the tube, at intervals of $l = 100$ mm.

The leading edge of the 532-nm laser pulse, henceforth called the "incident laser beam", emerged from the other side of the SBS amplifier cell. This beam was focused by a lens of focal length $f = 130$ mm and sent into a SBS generator cell filled with deionized water. The cell was a quartz tube of diameter $d = 40$ mm and length $l = 200$ mm, with fused silica windows (identical to the ones in the above amplifier cell) attached to the two ends. The beam focus was positioned in the water, close to the entrance window. The water was constantly circulated through the cell and the above filter, and this removed any residual particles in the water which could cause sparks in the beam focus. The power density was here so high that strong acoustic waves were generated in the water. These phonons then acted as a phase-conjugating mirror, such that a SBS Stokes beam emerged from the focus with the opposite phase and propagation direction to the original incident beam. The SBS beam reentered the amplifier cell as a parallel beam, and beat with the counterpropagating part of the incident laser beam. This creating a strong acoustic wave that propagated collinearly with the SBS beam. Successive sections of the incident laser beam reflected off the leading edge of this growing acoustic wave. The intensity of the SBS laser light therefore increased coherently as it

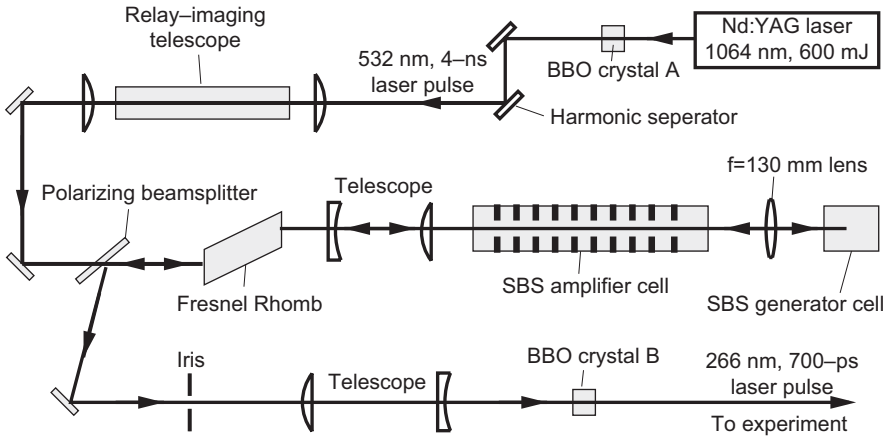

Fig. 7. Schematic diagram of pulsed UV laser system. The output of a Nd:YAG laser was frequency-doubled in BBO crystal A to generate a 4-ns-long laser pulse of wavelength $\lambda = 532$ nm and energy $E = 280$ mJ. This beam was sent into a Stimulated Brillouin Scattering (SBS) amplifier cell and a SBS generator cell, thereby shortening its pulse-length to $\Delta t \sim 700$ ps (see text). This laser pulse was frequency-doubled by BBO crystal B to generate 266-nm laser pulses.

propagated along the tube, while its pulse length was compressed.

The amplified SBS beam exited the cell and reentered the Fresnel Rhomb, thereby becoming vertically polarized. The beam was then diverted from the path of the incident laser beam by the above polarizing beam splitter. The diameter of the SBS beam was here $d\sim 8$ mm, and we used an iris of $d\sim 3$ mm to select the central part of the beam. The pulse duration in this central part was typically short ($\Delta t\sim 700$ ps) [63], whereas the outer, removed parts had values $\Delta t > 1.5$ ns. This beam image was then transferred to the position of a 6-mm-long BBO crystal (B in Fig. 7), using a pair of relay-imaging lenses and a vacuum tube with Brewster windows. The crystal was cut for type-I frequency doubling and generated a 266-nm laser beam of energy $E\sim 5$ mJ.

The time profile of the laser pulse was measured using a p–i–n photodiode and the above 3-GHz digital oscilloscope. The full-width-at-half-maximum (FWHM) duration of the laser pulses were typically around $\Delta t\sim 700$ ps, as shown in the trace of Fig. 6(c). The laser energy per pulse was measured with an absolute precision of ~10% using pyroelectric and calorimetric detectors. Shot-to-shot fluctuations in the energy were typically around ±30%, presumably caused by fluctuations during the SBS process.

6. Measurements with UV laser beam

We next replaced the carbon target foil of Fig. 2 with the gold photocathode described above, and irradiated it with the UV laser beam to generate photoelectrons. This simulated the monitor response against the secondary electrons produced by the Linac4 beam. The gold photocathode was cleaned before use by (i) placing it in an ultrasonic bath filled with acetone, (ii) heating it to temperature $T = 100\,^{\circ}$C in vacuum for several hours, (iii) cooling it to room temperature and evacuating it to pressure $P = 10^{-7}$ Pa, (iv) irradiating it for ~3 h with a 266-nm laser beam of power density $\rho\sim 10\,\mathrm{MW\,cm^{-2}}$. This "activated" the photocathode, i.e., cleaned it by UV photon bombardment [69,70]. All of the measurements described below were carried out by placing the monitor next to the RFQ Decelerator (RFQD) of AD [14,71], which was excited at frequency $f = 202.5$ MHz. This tested whether the monitor could be used in the electromagnetic interference produced by a RFQ or synchrotron. No such interference was observed in the CCD images.

The photoelectrons were produced by irradiating the photocathode with UV laser energies $E = 10-200\,\mu$J. A pair of plano-convex lenses of focal lengths $f = 300$ and 500 mm adjusted the diameter of the laser beam on the photocathode to values between $d = 3$ and 10 mm. The number of photoelectrons $N_\gamma = 2\times 10^7 - 4\times 10^8$ emitted per incident laser pulse was measured by using a digital oscilloscope to record the charge induced on the photocathode. At these power densities of the 4.7-eV laser photons, the photoelectron emission proceeds via a linear, single-photon absorption [69,70], whereas the contribution from any multiphoton process is negligible. Indeed, the N_γ-values measured here increased linearly with the laser intensity. The quantum efficiency $\gamma\sim 5\times 10^{-6}$ was within an order of magnitude of published values [69,70]. The yield N_γ began to saturate, however, at high power densities $\rho > 1\,\mathrm{MW\,cm^{-2}}$ of the laser. Past studies [69,70] also observed this saturation, which was attributed to space-charge effects at the foil surface.

We began these tests by measuring the spatial resolution of the monitor. Fig. 8(b) shows a contour plot of the profile of a UV laser beam measured by the monitor. The vertical and horizontal cross-sections of this profile at $x = -3$ mm and $y = -1$ mm, respectively, are shown in Figs. 8(a) and (c). The UV beam at the position of the photocathode had horizontal and vertical FHWM diameters $d_h = 3$ mm and $d_v = 1.5$ mm, and its intensity was adjusted to yield $N_e\sim 5\times 10^7$ photoelectrons per laser pulse. The CCD was exposed over a single laser pulse. The two ring magnets of Fig. 2 were removed for these measurements (i.e., $B = 0$), and the electrode voltages were adjusted to the settings 1 of Table 2. The potentials $V_f = -3$ kV and $V_p = 6.5$ kV used here implied a kinetic energy $E = 9.5$ kV for the photoelectrons striking the phosphor screen. The spatial resolution of the monitor was expected to improve at these high acceleration voltages [72]. The CCD image (Fig. 8) obtained in this way consisted of a bright spot, with horizontal and vertical diameters $d_h\sim 3.5$ mm and $d_v\sim 2$ mm. This indicates that the spatial resolution of the monitor was around $\Delta x\sim 2$ mm. The image of Fig. 8(b) also contained a constant background of counts over the entire CCD frame, with an intensity of a few percent relative to the main signal. This background was presumably caused by light scattered within the phosphor screen and at the interfaces between the optical conduits.

We next studied the time resolution of the monitor, and its relationship with the beam images measured by the CCD. In Fig. 9, a sequence of 12 CCD images taken at various trigger timings between $t = -5$ and 50 ns of the monitor electrodes, relative to the arrival of the laser pulse at $t = 0$, is shown. The measurements were carried out using the voltage settings 2 of Table 2. The two ring magnets of Fig. 2 were installed to produce an axial field $B\sim 100$ Gauss between the foil and phosphor screen. The diameter of the laser beam on the photocathode was adjusted to $d = 6$ mm, and each laser pulse produced $N_e = 4\times 10^8$ photoelectrons. The CCD image measured in this way at $t = -5$ ns showed a beam diameter $d\sim 6$ mm (Fig. 9(a)). At $t = -4$ ns, the intensity of the CCD image dimmed. At $t = 0$ ns, a stronger flash of diameter $d\sim 6$ mm was observed (Fig. 9(c)). A weak afterpulse continued for tens of nanoseconds after this main pulse. Between $t = 2$ and 6 ns, a structure was observed in the afterpulse, which rotated clockwise (Figs. 9(d)–(h)) with a rotation frequency of a few hundred MHz. This corresponded to the cyclotron frequency of an electron in a magnetic field $B\sim 100$ Gauss. The diameter of the profile gradually increased as it

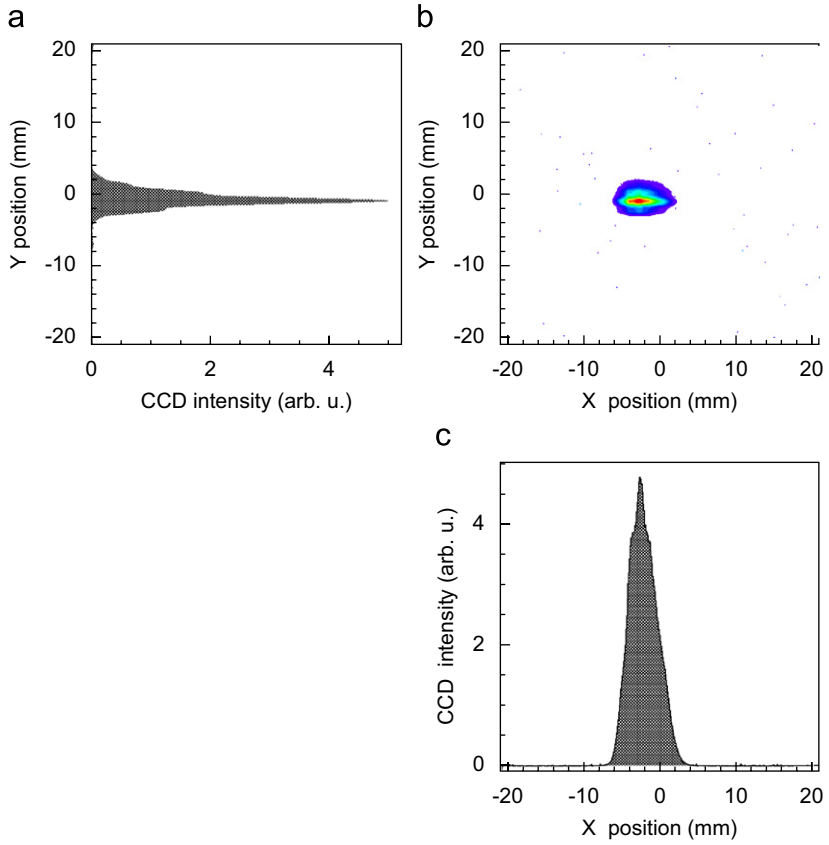

Fig. 8. Contour plot of the spatial beam profile of a UV laser pulse measured by the monitor (b). The vertical (a) and horizontal (c) cross-sections of this profile at $x = -3$ mm and $y = -1$ mm, respectively. The voltage settings 1 of Table 2 were used in these measurements. The constant background on the CCD readout has been subtracted here.

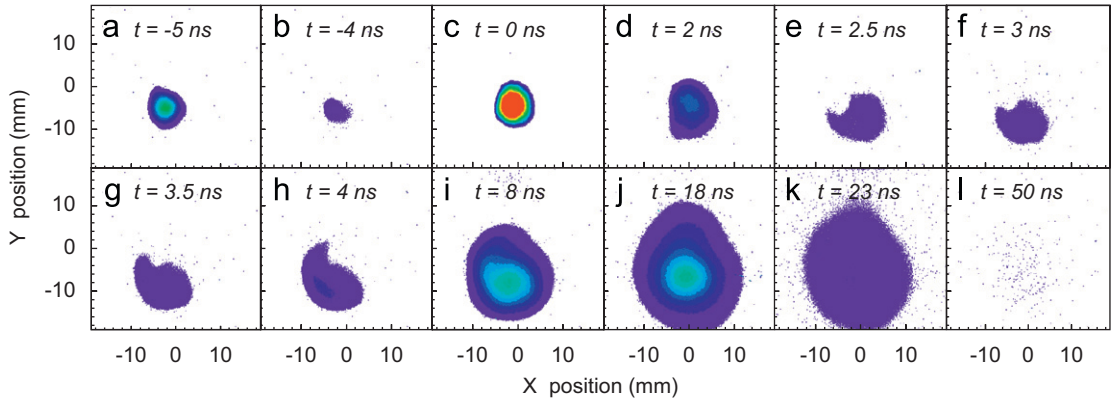

Fig. 9. Sequence of CCD exposures taken by irradiating the photocathode with UV laser pulses which released $N_e \sim 4 \times 10^8$ photoelectrons per laser pulse. The voltage settings 2 of Table 2 and a magnetic field $B = 100$ Gauss were used. The timings of the electrode gates [indicated in each figure (a)–(l)] were adjusted between $t = -5$ and 50 ns, relative to the arrival time of the laser pulse.

rotated, to $d \sim 10-15$ mm at $t = 18-23$ ns. The afterpulse nearly disappeared at $t \sim 50$ ns (Fig. 9(j)).

In Fig. 10, the measured intensities of the CCD images of Figs. 9(a)–(j) are plotted as a function of the gating time t, which was incremented in steps of $\Delta t = 250$ ps. As expected, a strong peak is seen at $t = 0$, corresponding to the arrival of the laser-induced photoelectrons at the phosphor screen. The FWHM width of this peak was around $\Delta t = 1.5$ ns. This value, relative to the 700-ps duration of the UV laser pulse (Fig. 6(c)), reflected the time resolution of the monitor. In Fig. 10, four spurious afterpulses are seen at $t \sim 9$, 18, 27, 36, and 45 ns, of gradually decreasing intensity. From the constant interval $\Delta t \sim 9$ ns between these afterpulses, and the rotating behavior of their spatial profile in Figs. 9(d)–(i), we conclude that the afterpulses occur when electrons are trapped by the magnetic field and make several round trips between the monitor electrodes. Indeed, particle-trajectory

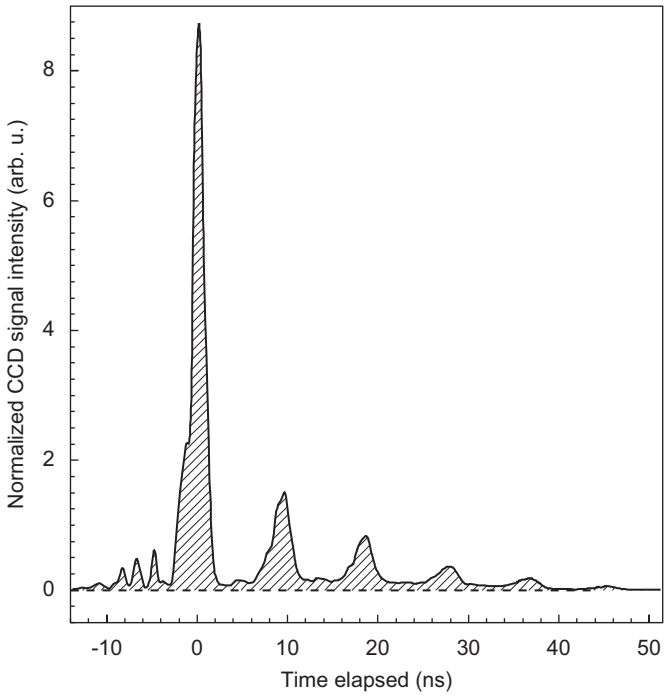

Fig. 10. Time profile of the UV laser pulse measured by the monitor, at an intensity corresponding to $N_e = 4 \times 10^8$ photoelectrons. The timings t of the electrode gates were scanned relative to the arrival time of the laser pulse, and the intensity of the CCD signal at each t was plotted. The voltage settings 2 of Table 2, and a magnetic field $B = 100$ Gauss were used.

simulations which include space-charge effects show that some of the electrons emitted from the target foil or grid A can be accelerated to grid B and reach grid D, and then reflect back to grid A with a frequency of around $f \sim 100$ MHz. Electrons produced by the ionization of residual gases in the chamber or by secondary electron emission from the grids when the photoelectrons strike them, can also follow similar trajectories. All these trapped electrons can then strike the phosphor screen when it is gated on, thereby producing the afterpulses.

Fig. 10 also reveal several prepulses in the time spectrum at $t = -9$, -7, and -5 ns. The voltage gate applied to grid D was normally expected to remove these prepulses by stopping the flow of signal electrons, thereby defining the end of the phosphor exposure (Fig. 6(b)). The fact that the prepulses are nevertheless observed indicates that some of the electrons managed to pass through the potential barrier of grid D after the gate was closed. As shown in Fig. 6(b), the waveform of the HV pulse applied to grid D contains noise of large amplitude; this may allow some of the electrons to traverse grid D at certain timings.

We attempted to suppress the prepulses and afterpulses by using the voltage settings 3 of Table 2 wherein, (i) the magnetic field was removed, (ii) the kinetic energy of the photoelectrons passing through grid D was reduced by increasing the photocathode voltage V_f, (iii) the height of the potential barrier V_D was increased, (iv) the acceleration voltage on the phosphor screen V_p was reduced. The time profile of Fig. 12(a) was obtained using these new settings, all other conditions (laser beam diameter and number of photoelectrons N_e) being identical to those of Fig. 10. The amplitudes of the prepulses and afterpulses have now been greatly reduced, to around 3% of the main pulse.

In Figs. 11(a)–(f), the spatial profiles corresponding to the time profile of Fig. 12(a), measured at CCD trigger timings between $t = -2$ and 3 ns, are shown. Although the laser beam on the photocathode was adjusted to vertical and horizontal diameters $d_v \sim 8$ mm and $d_h \sim 3$ mm, the CCD images were much larger ($d \sim 15$ mm). This blow-up is due to space-charge effects in the photoelectron beam during transport from the photocathode to the phosphor screen. Several vertical and horizontal bands are seen in Figs. 11(c)–(d), which were presumably caused by the deflection of the photoelectron trajectories near the grid filaments during the blow-up. The photoelectrons were multiplied when they struck the acceleration grids, and this could also contribute to this band structure.

To avoid these space-charge effects, we used a lower intensity in the UV laser, corresponding to $N_e = 2 \times 10^7$ photoelectrons emitted from the photocathode per laser pulse. The spatial profiles measured at these conditions are shown in Figs. 11(g)–(k). The band structure and blow-up have now been reduced. The relative amplitude of the afterpulses are also much smaller; as shown in the corresponding time profile of Fig. 12(b), they are ~0.5% of the main pulse.

7. Measurements with proton beam

We next carried out an experiment using the tandem facility of the Institut de Physique Nucléaire, Orsay, to study the response of the monitor against a 3-MeV proton beam. The tandem provided 5-ns-long micro-bunches containing $N_p = 5 \times 10^4$ protons, which arrived at the monitor with a repetition rate $f_r = 10$ MHz. During the measurements described below, the acceleration grids and phosphor screen were gated on for duration $\Delta t = 1$ ns, repetitively and in synchronization with the micro-bunch arrivals. The CCD was typically exposed for 1–6 min, during which the signals of 10^2–10^3 micro-bunches of protons were integrated on it. Previous studies had shown that the secondary electron emission yield for 3-MeV protons striking a graphite target is around $\Gamma \sim 0.7$ [73,74]. In the present monitor, each proton micro-bunch was measured to produce $N_e = (2-3) \times 10^4$ secondary electrons, in rough agreement with the expected value $N_e \sim N_p \Gamma$.

The imaging performance of the monitor was studied by using the quadrupole magnets in the tandem beamline to vary the shape of the proton beam on the foil. In Figs. 13(a)–(d), the images recorded by the monitor for a circular beam of diameter $d = 5$ and 15 mm, and horizontal and vertical slit-like beams, are shown. The spatial resolution for cases wherein the secondary electrons were accelerated between the foil and phosphor with an energy

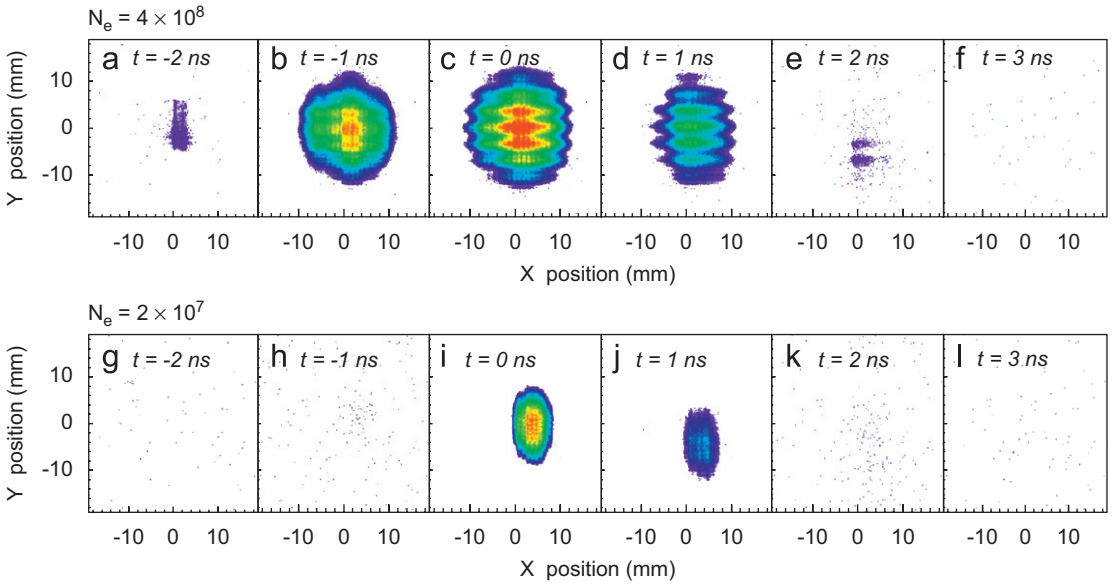

Fig. 11. Sequence of CCD exposures taken of the UV laser pulses, using the electrode voltage settings 3 of Table 2. Profiles (a)–(f) were measured at a photoelectron intensity $N_e = 4 \times 10^8$, whereas (g)–(l) were measured at $N_e = 2 \times 10^7$.

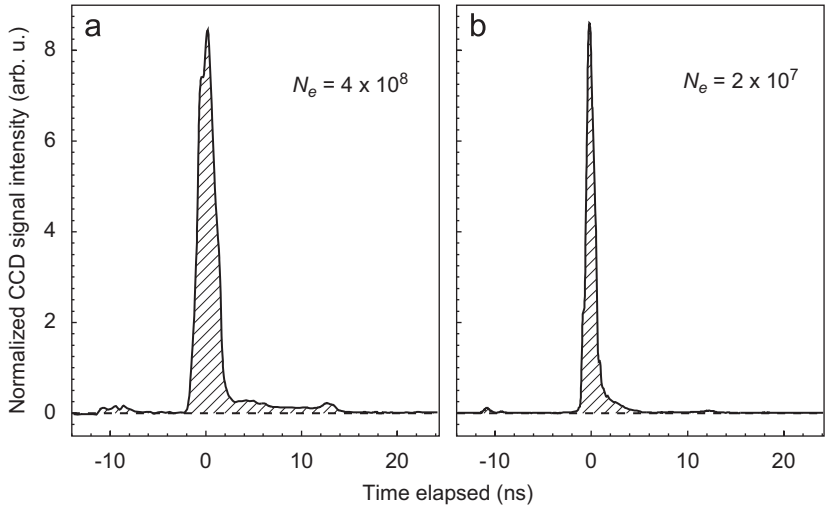

Fig. 12. Time profile of the UV laser pulse measured by the monitor, at an intensity corresponding to $N_e = 4 \times 10^8$ (a) and $N_e = 2 \times 10^7$ (b) photoelectrons. The voltage settings 3 of Table 2 were used, and the permanent magnets removed ($B = 0$). Note that the signal intensity of (a) is greater than that of (b) by an order of magnitude, whereas we here plot the normalized intensities.

$E = 8$ keV was $\Delta x < 2$ mm. Space-charge effects at these low beam intensities induced negligible blow-up in the CCD image. This is in good agreement with the results of particle-tracking simulations.

We next studied the dynamic range of the monitor, by measuring its response against a 10-mm-diameter proton beam of various intensities, between $N_p = 10$ and 6×10^4 protons per micro-bunch. In Figs. 14(a)–(b), the amplitude of the signal measured by the CCD is plotted as a function of the proton intensity N_p calibrated by a Faraday cup. A linear response was observed over the four orders of magnitude in beam intensity that was accessible by the tandem, within the systematic error of the Faraday cup readings. Clear signals were observed at the lowest proton intensities $N_p \sim 10$.

8. Conclusions and discussions

We have described a beam profile monitor which imaged the secondary electrons emitted from a thin target foil, using a phosphor screen and CCD. Systematic measurements indicated that the monitor satisfied the requirements for use in the 3-MeV beam of the planned Linac4 RFQ. The monitor constituted a "stop motion camera" for beams with nanosecond-scale time structures. Its response against UV laser pulses of 700-ps duration which released

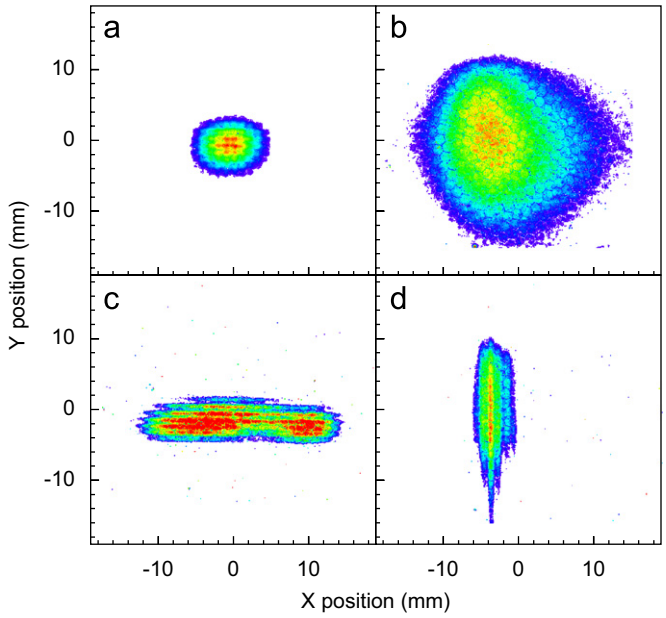

Fig. 13. Spatial profiles of the 3-MeV tandem beam containing $N_p \sim 5 \times 10^4$ protons per micro-bunch, measured for circular beams of diameter $d = 5$ mm (a) and 15 mm (b), and beams that were horizontally (c) and vertically (d) elongated. The electrode voltage settings 1 of Table 2 were used, with no magnetic field. The measurements were made by integrating the signals from 120 micro-bunches on the CCD.

between $N_e \sim 2 \times 10^7$ and 4×10^8 photoelectrons from the foil within 1 ns, was studied. A time resolution $\Delta t \sim 1$ ns was attained by applying HV pulses of sub-nanosecond rise and fall times on several electrodes, which controlled the flow of secondary electrons between the foil and phosphor. Spurious prepulses and afterpulses appeared in the measured time profiles of the beam. The amplitudes of these could be reduced to around 0.5% of the main pulse, by lowering the acceleration voltages of the signal electrons, and increasing the potential amplitudes on the grid used to interrupt them. The relative intensities of the prepulses and afterpulses increased at high beam intensities (e.g., $N_e = 4 \times 10^8$ electrons emitted within $\Delta t \sim 1$ ns from a ~5-mm-diameter spot on the photocathode), due to space-charge effects.

The spatial resolution of the monitor was typically around $\Delta x \sim 2$ mm, when the signal electrons were transported with acceleration energies $E = 8-9$ keV between the foil and phosphor screen. This resolution deteriorated to $\Delta x > 10$ mm, when the acceleration voltage was decreased to a few hundred volts and high photoelectron intensities (e.g., $N_e \sim 4 \times 10^8$) were used. The results imply that the monitor should be operated in two modes, depending on the purpose of the measurement: one using high acceleration voltages to optimize the spatial resolution, and the other with low voltages to suppress the prepulses and afterpulses.

The sensitivity and linearity of the monitor was studied using 5-ns-long beam pulses containing between $N_p \sim 10$ and 6×10^4 protons of energy $E = 3$ MeV. The response was linear over these four orders of magnitude. By varying

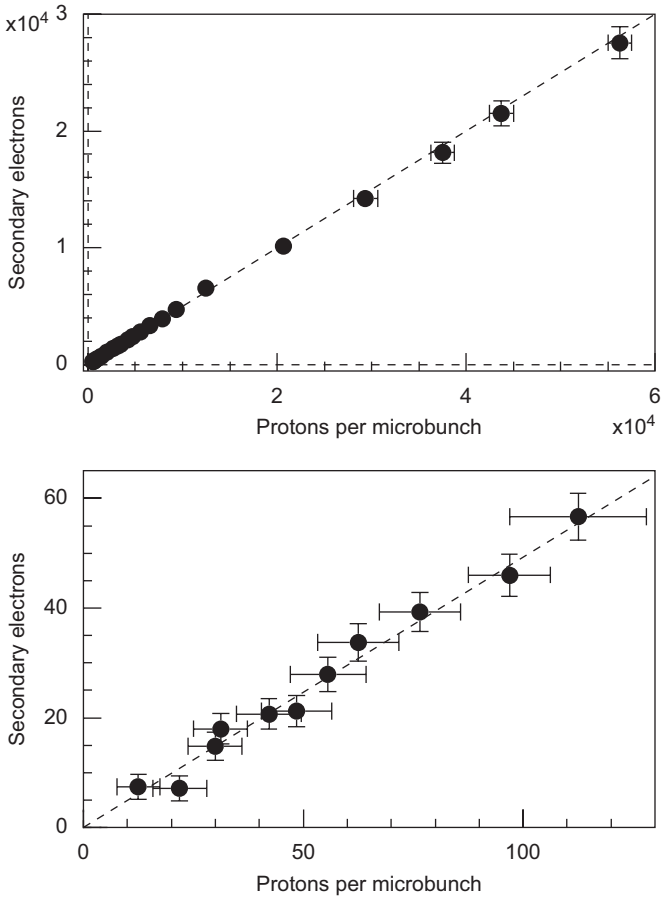

Fig. 14. Intensity of the CCD signals, as a function of the number of 3-MeV protons in each 5-ns-long micro-bunch arriving at the carbon foil. The measurements were made by using the voltage settings 3 of Table 2, and integrating the signals from 10^3 micro-bunches on the CCD.

the expose time of the CCD and triggering the monitor electrodes many times in synchronization with the arrival of repetitive beam pulses, the dynamic range and sensitivity of the monitor against these pulses was increased by many orders of magnitude. Indeed, these laser and proton tests indicated that the monitor can be used over a range of 6–7 orders of magnitude in beam intensity, corresponding to between $N_e \sim 5$ and 4×10^8 electrons per pulse. The sensitivity of the monitor against the transverse beam halo in the RFQ beam may be improved by allowing the main part of the H^- beam to pass through a suitable hole in the carbon target foil, and intercepting only the halo.

Although the monitor performance is now adequate for use in the initial phase of the Linac4 development which involves H^- injection into the PSB, the device must be further improved if it is to be used in the future SPL facility. The largest problem is the space-charge effect [72] in the secondary electrons at high intensities of the Linac4 beam, and the large prepulses and afterpulses induced by this. One possibility for reducing these spurious pulses may be to add more switching electrodes to the monitor. Indeed, we had previously studied the afterpulses that occur in gated photomultipliers [26,75]. By switching the

potentials of the photocathode and four dynodes simultaneously, we suppressed the intensity of the afterpulses to 5×10^{-4} relative to the main pulse. In this earlier study we also found that the amplitudes of the afterpulses increase (up to ~3% of the main pulse), at high gains ($\sim 4 \times 10^6$) of the photomultiplier. Afterpulses in photomultipliers had been experimentally [77–83] and theoretically [76] studied over a period of 40 years. It is predominantly produced by electrons which ionize the residual gas in the volume between the photocathode and dynodes. The positive ions drift towards the photocathode and strike its surface, releasing secondary electrons. These electrons are then accelerated towards the anode and create the afterpulse. Similar effects can occur when electrons strike the photomultiplier dynodes and release positive ions from their surface.

The residual gases (mostly hydrogen, nitrogen, and water) in the monitor chamber at pressure $P \sim 5 \times 10^{-7}$ Pa can similarly be ionized by the signal electrons. Contamination (e.g., water and oil) on the filaments, carbon foil, and phosphor screen are difficult to remove, and these also readily emit positive ions when bombarded by the signal electrons. It may therefore be difficult to completely suppress the afterpulses below a relative intensity of $10^{-3} - 10^{-4}$ by using switched electrodes alone.

An alternative way of eliminating the space-charge problems and the prepulses and afterpulses may be to avoid intercepting the ion beam with a target foil or filament. Instead, the laser system of Fig. 7 could be employed to photoneutralize the 3-MeV H^- ion beam, and then the emerging photoelectrons transported to the present monitor to provide the spatial and time profiles of the beam. The 700-ps-long laser pulse would be fired into the monitor in synchronization to the RF of Linac4, to selectively irradiate the interesting parts of the beam. Since the laser pulse defines the time resolution of the monitor, such a system would avoid some of the problems of space-charge and delayed electrons encountered in the present work.

Acknowledgements

We are deeply indebted to F. Caspers, A. Dax, R. Garoby, J.D. Hares, R.S. Hayano, T. Komaba, J.-B. Lallement, T. Lefevre, A. Lombardi, M. Mitani, C. Rossi, E.Z. Sargsyan, A. Sótér, and M. Vretenar for their invaluable help and encouragement. The construction and tests of the monitor using the UV laser beam were carried out at the ASACUSA beamline of CERN's Antiproton Decelerator. We thank the Tandem staff of IPN, Orsay for their great efforts in providing a stable proton beam. This work was supported by the European Community-Research Infrastructure Activity (CARE, RII3-CT-2003-506395), the Grant-in-Aid for Creative Basic Research (10NP0101) of Monbukagakusho, the Japan Society for Promotion of Science, and the European Young Investigator Awards (EURYI) of the European Science Foundation and the Deutsche Forschungsgemeinschaft (DFG).

References

[1] L. Arnaudon, et al., Linac4 Technical Design Report, CERN-AB-2006-084 ABP/RF, CERN, Geneva, 2006.
[2] C. Rossi, L. Bruno, F. Caspers, R. Garoby, J. Genest, K. Hanke, M. Hori, D. Kuchler, A. Lombardi, M. Magistris, A. Millich, M. Paoluzzi, E. Sargsyan, M. Silari, T. Steiner, M. Vretenar, The SPL front end: A 3 MeV H^- test stand at CERN, in: Proceedings of LINAC 2004, Lübeck, Germany, 2004.
[3] M. Vretenar, G. Bellodi, R. Garoby, F. Gerigk, K. Hanke, A.M. Lombardi, S. Maury, M. Pasini, C. Rossi, E.Z. Sargsyan, Linear accelerator designs for the upgrade of the CERN proton injector complex (Linac4, SPL), in: Proceedings of the Asian Particle Accelerator Conference 2007, Indore, India, 2007.
[4] F. Gerigk, et al., Conceptual design of the SPL II—a high-power superconducting H^- linac at CERN, CERN-2006-006, CERN, Geneva, 2006.
[5] W. Weterings, G. Bellodi, J. Borburgh, T. Fowler, F. Gerigk, B. Goddard, K. Hanke, M. Martini, L. Sermeus, 160 MeV H^- injection into the CERN PSB, in: Proceedings of Particle Accelerator Conference 2007, Albuquereque, New Mexico, 2007.
[6] T. Kroyer, F. Caspers, E. Mahner, The CERN SPL Chopper Structure—a Status Report, CARE-Report-2006-033-HIPPI, CERN, Geneva, 2007.
[7] C.K. Allen, K.C.D. Chan, P.L. Colestock, K.R. Crandall, R.W. Garnett, J.D. Gilpatrick, W. Lysenko, J. Qiang, J.D. Schneider, M.E. Schulze, R.L. Sheffield, H.V. Smith, T.P. Wangler, Phys. Rev. Lett. 89 (2002) 214802.
[8] T.P. Wangler, K.R. Crandall, R. Ryne, T.S. Wang, Phys. Rev. ST Accel. Beams 1 (1998) 084201.
[9] D. Jeon, J. Stovall, A. Aleksandrov, J. Wei, J. Stalpes, R. Keller, L. Young, H. Takeda, S. Nath, Phys. Rev. St Accel. Beams 5 (2002) 094201.
[10] R. Ferdinand, P.-Y. Beauvais, R. Duperrier, A. France, J. Gaiffier, J.-M. Lagniel, M. Painchault, F. Simoens, P. Balleyguier, Status Report on the 5 MeV IPHI RFQ, in: Proceeding of the LINAC 2000 Conference, Monterey, CA, 2000.
[11] A.M. Lombardi, E.Z. Sargsyan, S. Lanzone, J.-B. Lallement, G. Bellodi, M. Baylac, R. Duperrier, D. Uriot, End-to-end beam dynamics for CERN Linac4, in: Proceedings of the 39th ICFA Advanced Beam Dynamics Workshop on High Intensity High Brightness Hadron Beams, Tsukuba, Japan, 2006.
[12] J. Wei, The spallation neutron source project—physical and technical challenges, in: Proceedings of the 2002 European Particle Accelerator Conference, Paris, France, 2002.
[13] M. Hori, Rev. Sci. Instrum. 76 (2005) 113303.
[14] M. Hori, J. Eades, R.S. Hayano, T. Ishikawa, W. Pirkl, E. Widmann, H. Yamaguchi, H.A. Torii, B. Juhász, D. Horváth, T. Yamazaki, Phys. Rev. Lett. 91 (2003) 123401.
[15] M. Hori, J. Eades, R.S. Hayano, T. Ishikawa, J. Sakaguchi, E. Widmann, H. Yamaguchi, H.A. Torii, B. Juhász, D. Horváth, T. Yamazaki, Phys. Rev. Lett. 87 (2001) 093401.
[16] P. Belochitskii, Status of the antiproton decelerator and of the ELENA project at CERN, in: Proceedings of COOL 2007, Bad Kreuznach, Germany, 2007.
[17] M.-E. Angoletta, M. Barnes, A. Beuret, P. Belochitskii, J. Borburgh, P. Bourquin, M. Buzio, D. Cornuet, T. Eriksson, T. Fowler, M. Hori, E. Mahner, S. Maury, D. Mohl, J. Monteiro, S. Pasinelli, F. Pedersen, U. Raich, L. Soby, P. Strubin, G. Tranquille, T. Zickler, ELENA—a preliminary cost and feasibility study, CERN-AB-2007-079 OP, CERN, Geneva, 2007.
[18] E. Widmann, FLAIR, a facility for low-energy antiproton and ion research, in: Low Energy Antiproton Physics: Eighth International

Conference on Low Energy Antiproton Physics (LEAP '05), AIP Conference Proceedings vol. 796, 2005, p. 385.
[19] A.N. James, T.P. Morrison, K.L. Ying, K.A. Connell, H.G. Price, J. Simpson, Nucl. Instr. and Meth. A 267 (1988) 144.
[20] D. Shapira, T.A. Lewis, L.D. Hulett Jr., Z. Ciao, Nucl. Instr. and Meth. A 449 (2000) 396.
[21] D. Shapira, T.A. Lewis, L.D. Hulett, Nucl. Instr. and Meth. A 454 (2000) 409.
[22] P.N. Ostroumov, P. Billquist, M. Portillo, W.Q. Shen, Rev. Sci. Instrum. 73 (2002) 56.
[23] A.R. Faruqi, Nucl. Instr. and Meth. A 439 (2000) 606.
[24] E. Peli, W.P. Siegmund, J. Opt. Soc. Am. A 12 (1995) 2274.
[25] C.J. Pawley, A.V. Deniz, Rev. Sci. Instrum. 71 (2000) 1286.
[26] M. Hori, K. Yamashita, R.S. Hayano, T. Yamazaki, Nucl. Instr. and Meth. A 496 (2003) 102.
[27] T. McCarville, S. Fulkerson, R. Booth, J. Emig, B. Young, S. Anderson, B. Heeter, Rev. Sci. Instrum. 76 (2005) 103501.
[28] Z. Yingji, W. Yongqin, W. Qiuyu, Q. Wenguo, Nucl. Instr. and Meth. A 302 (1991) 76.
[29] O.H. Odland, W. Mittig, A. Lépine-Szily, G. Fremont, M. Chartier, M. MacCormick, J.M. Casandjian, Nucl. Instr. and Meth. A 378 (1996) 149.
[30] G. Montagnoli, et al., Nucl. Instr. and Meth. A 547 (2005) 455.
[31] O.H.W. Siegmund, M. Lampton, R. Raffanti, W. Herrick, Nucl. Instr. and Meth. A 310 (1991) 311.
[32] O. Jagutzki, V. Mergel, K. Ullmann-Pfleger, L. Spielberger, U. Spillmann, R. Dörner, H. Schmidt-Böcking, Nucl. Instr. and Meth. A 477 (2002) 244.
[33] P.V. Schmidt, L. Willmann, R. Abela, J. Bagaturia, W. Bertl, B. Braun, H. Folger, K. Jungmann, D. Mzavia, G. zu Putlitz, D. Renker, T. Sakhelashvilli, L. Zhang, Nucl. Instr. and Meth. A 376 (1996) 139.
[34] J.S. Lapington, Nucl. Instr. and Meth. A 392 (1997) 336.
[35] S. Coeck, M. Beck, B. Delauré, V.V. Golovko, M. Herbane, A. Lindroth, S. Kopecky, V.Yu. Kozlov, I.S. Kraev, T. Phalet, N. Severijns, Nucl. Instr. and Meth. A 557 (2006) 516.
[36] J.D. Gilpatrick, D. Barr, L.A. Day, D.M. Kerstiens, M. Stettler, R. Valdiviez, M. Gruchalla, J.F. O'Hara, J.H. Kamperschroer, Beam-profile instrumentation for beam-halo measurement: overall description and operation, in: Proceedings of the 2001 Particle Accelerator Conference, Chicago, IEEE, Piscataway, NJ, 2001.
[37] A. Browman, M. Borden, D. Fitzgerald, R. Macek, R. McCrady, T. Spickermann, T. Zaugg, Halo measurements of the extracted beam at the Los Alamos proton storage ring, in: Proceedings of the 2003 Particle Accelerator Conference, Portland, IEEE, Piscataway, NJ, 2003.
[38] N. Hayashi, S. Hiroki, J. Kishiro, Y. Teruyama, R. Toyokawa, D. Arakawa, S. Lee, T. Miura, T. Toyama, Development of the beam diagnostics system for the J-PARC rapid-cycling synchrotron, in: Proceedings of 2005 Particle Accelerator Conference, Knoxville, TN, IEEE, Piscataway, NJ, 2005.
[39] S.G. Arutunian, N.M. Dobrovolski, M.R. Mailian, I.E. Vasiniuk, Phys. Rev. ST Accel. Beams 6 (2003) 042801.
[40] R. Connolly, P. Cameron, J. Cupolo, M. Grau, M. Kesselman, C.-J. Liaw, R. Sikora, Laser profile measurements of an H^- beam, in: Proceedings of the 2001 Particle Accelerator Conference, Chicago, IEEE, Piscataway, NJ, 2001.
[41] S. Assadi, A. Aleksandrov, W. Blokland, A. DeCarlo, C. Deibele, P. Gibson, W. Grice, M. Hechler, T. Hunter, J. Kelly, P. Ladd, G. Murdoch, M. Plum, J. Pogge, K. Potter, D. Purcell, T. Shea, D. Stout, The SNS laser profile monitor design and implementation, in: Proceedings of the 2003 Particle Accelerator Conference, Portland, IEEE, Piscataway, NJ, 2003.
[42] S. Lee, T. Tomisawa, H. Akikawa, Z. Igarashi, S. Sato, T. Toyama, A. Ueno, Y. Kondo, M. Ikegami, K. Hasegawa, Direct measurements of space-charge potential in high intensity H^- beam with laser based photo neutralization method, in: Proceedings of DIPAC 2005, Lyon, France.
[43] T. Tomisawa, H. Akikawa, S. Sato, A. Ueno, Y. Kondo, H. Oigawa, T. Sasa, K. Hasegawa, Investigation of photo neutralization efficiency of high intensity H^- beam with Nd:YAG laser in J-PARC, in: Proceedings of DIPAC 2005, Lyon, France.
[44] R. Connolly, R. Michnoff, T. Moore, T. Shea, S. Tepikian, Nucl. Instr. and Meth. A 443 (2000) 215.
[45] R. Connolly, R. Michnoff, S. Tepikian, Residual-gas-ionization beam profile monitors in RHIC, in: Proceedings of the 2005 Particle Accelerator Conference, Knoxville, TN, IEEE, Piscataway, NJ, 2005.
[46] J. Dietrich, V. Kamerdzhiev, N.Ya. Rukhlyada, Instrum. Exp. Tech. (Engl. Transl.) 46 (2003) 581.
[47] J. Amundson, W. Pellico, L. Spentzouris, P. Spentzouris, T. Sullivan, Nucl. Instr. and Meth. A 570 (2007) 1.
[48] M. Hori, Nucl. Instr. and Meth. A 522 (2004) 420.
[49] P. Elmfors, A. Passó, M. Huhtinen, M. Lindroos, J. Olsfors, U. Raich, Nucl. Instr. and Meth. A 396 (1997) 13.
[50] S. Igarashi, D. Arakawa, K. Koba, H. Sato, T. Toyama, M. Yoshii, Nucl. Instr. and Meth. A 482 (2002) 32.
[51] C.J. Liaw, P.R. Cameron, Carbon wire heating due to scattering in the SNS, in: Proceedings of the 2001 Particle Accelerator Conference, Chicago, IEEE, Piscataway, NJ, 2001.
[52] M.J. Eckart, R.L. Hanks, J.D. Kilkenny, R. Pasha, J.D. Wiedwald, J.D. Hares, Rev. Sci. Instrum. 57 (1986) 2046.
[53] J.D. Kilkenny, P. Bell, R. Hanks, G. Power, R.E. Turner, J. Wiedwald, Rev. Sci. Instrum. 59 (1988) 1793.
[54] M. Katayama, M. Nakai, T. Yamanaka, Y. Izawa, S. Nakai, Rev. Sci. Instrum. 62 (1990) 124.
[55] D.K. Bradley, P.M. Bell, J.D. Kilkenny, R. Hanks, O. Landen, P.A. Jaanimagi, P.W. McKenty, C.P. Verdon, Rev. Sci. Instrum. 63 (1992) 4813.
[56] R.G. Watt, J. Oertel, T. Archeluta, Rev. Sci. Instrum. 65 (1994) 2585.
[57] J.A. Oertel, T.N. Archuleta, L.S. Schrank, Rev. Sci. Instrum. 72 (2001) 701.
[58] K.A. Wickersheim, R.V. Alves, R.A. Buchanan, IEEE Trans. Nucl. Sci. NS-17 (1970) 57.
[59] J.H. Chappell, S.S. Murray, Nucl. Instr. and Meth. 221 (1984) 159.
[60] J.P. Moy, A. Koch, M.B. Nielsen, Nucl. Instr. Meth. A 326 (1993) 581.
[61] G.C. Tyrrell, Nucl. Instr. and Meth. A 546 (2005) 180.
[62] D.M. Benzel, M.D. Pocha, Rev. Sci. Instrum. 56 (1985) 1456.
[63] S. Schiemann, W. Ubachs, W. Hogervorst, IEEE J. Quantum Electron. QE-33 (1997) 358.
[64] S. Schiemann, W. Ubachs, W. Hogervorst, IEEE J. Quantum Electron. QE-34 (1998) 407.
[65] D. Neshev, I. Velchev, W.A. Majewski, W. Hogervorst, W. Ubachs, Appl. Phys. B 68 (1999) 671.
[66] M. Hori, R.S. Hayano, E. Widmann, H.A. Torii, Opt. Lett. 28 (2003) 2479.
[67] M. Hori, A. Dax, J. Eades, K. Gomikawa, R.S. Hayano, N. Ono, W. Pirkl, E. Widmann, H.A. Torii, B. Juhász, D. Barna, D. Horváth, Phys. Rev. Lett. 96 (2006) 243401.
[68] M. Hori, J. Eades, R.S. Hayano, W. Pirkl, E. Widmann, H. Yamaguchi, H.A. Torii, B. Juhász, D. Horváth, K. Suzuki, T. Yamazaki, Phys. Rev. Lett. 94 (2005) 063401.
[69] T. Srinivasan-Rao, J. Fischer, T. Tsang, J. Appl. Phys. 69 (1991) 3291.
[70] T. Anderson, I.V. Tomov, P.M. Rentzepis, J. Appl. Phys. 71 (1992) 5161.
[71] A.M. Lombardi, W. Pirkl, Y. Bylinsky, First operating experience with the CERN decelerating RFQ for antiprotons, in: Proceedings of the 2001 Particle Accelerator Conference, Chicago, IEEE, Piscataway, NJ, 2001.
[72] J.-B. Lallement, E.Z. Sargsyan, M. Hori, Beam Shape and Halo Monitor Status, AB-Note-2006-047ABP, CERN, Geneva, 2007.
[73] H.P. Beck, R. Langkau, Z. Naturforsch. 30 (1975) 981.
[74] D. Hasselkamp, H. Rothard, K.-O. Groeneveld, J. Kemmler, P. Varga, H. Winter, Particle Induced Electron Emission II, Springer, Heidelberg, 1992.
[75] M. Hori, J. Eades, E. Widmann, T. Yamazaki, R.S. Hayano, T. Ishikawa, H.A. Torii, T. von Egidy, F.J. Hartmann, B. Ketzer, C. Maierl, R. Pohl, M. Kumakura, N. Morita, D. Horváth, I. Sugai, Phys. Rev. A 70 (2004) 012504.

[76] S. Ohsuka, Y. Ogata, Y. Tamura, Nucl. Instr. and Meth. A 384 (1997) 477.
[77] G.A. Morton, H.M. Smith, R. Wasserman, IEEE Trans. Nucl. Sci. NS-14 (1967) 443.
[78] R. Staubert, E. Böhm, K. Hein, K. Sauerland, J. Trümper, Nucl. Instr. and Meth. 84 (1970) 297.
[79] S.J. Hall, J. McKeown, Nucl. Instr. and Meth. 112 (1973) 545.
[80] P.B. Coates, J. Phys. D 6 (1973) 1159.
[81] B.H. Candy, Rev. Sci. Instrum. 56 (1985) 183.
[82] R. Mirzoyan, E. Lorenz, D. Petry, C. Prosch, Nucl. Instr. and Meth. A 387 (1997) 74.
[83] V.A. Morozov, N.V. Morozova, Instrum. Exp. Tech. (Engl. Transl.) 45 (2002) 685.